

Pristine Massive Star Formation Caught at the Break of Cosmic Dawn

Takahiro Morishita^{1*}, Zhaoran Liu², Massimo Stiavelli³,
Tommaso Treu⁴, Pietro Bergamini^{5,6}, Yechi Zhang¹

¹IPAC, California Institute of Technology, MC 314-6, 1200 E.
California Boulevard, Pasadena, 91125, CA, USA.

²Astronomical Institute, Graduate School of Science, Tohoku
University, 6-3 Aoba, Sendai, 980-8578, Miyagi, Japan.

³Space Telescope Science Institute, 3700 San Martin Drive, Baltimore,
21218, MD, USA.

⁴Department of Physics and Astronomy, University of California, Los
Angeles, 430 Portola Plaza, Los Angeles, 90095, CA, USA.

⁵Dipartimento di Fisica, Università degli Studi di Milano, Via Celoria
16, Milano, I-20133, Italy.

⁶INAF - OAS, Osservatorio di Astrofisica e Scienza dello Spazio di
Bologna, via Gobetti 93/3, Bologna, I-40129, Italy.

*Corresponding author(s). E-mail(s): takahiro@ipac.caltech.edu;

Abstract

The existence of galaxies with no elements such as Oxygen – formed by stars after Big Bang nucleosynthesis – is a key prediction of the cosmological model. Finding them would provide direct and transformative evidence of the formation of the first galaxies in extremely different conditions than those observed today. JWST has enabled the identification of galaxies all the way to cosmic times of a few hundred million years^[1–5]. However, no pristine “zero-metallicity” Population III galaxies have been identified so far. Here, we report the identification of an extremely metal-poor galaxy at redshift $z = 5.725$ (“AMORE6”), about one billion years after the Big Bang, observed near the critical line of a foreground galaxy cluster, and thus multiply imaged and magnified ($\mu = 39\text{--}78$). Publicly available JWST NIRCам Wide Field Slitless Spectroscopy (WFSS) spectra consistently detect $H\beta$ at both image positions, but $[O\ III]_{\lambda\lambda 4960,5008}$ remains undetected. This places

a firm upper limit on its oxygen abundance of $12 + \log(\text{O}/\text{H}) < 6.0$ (1σ), or $< 0.20\%$ of solar metallicity. AMORE6 is characterized by low stellar mass ($5.6^{+0.2}_{-0.1} \times 10^5 M_\odot$), very blue rest-frame UV spectral slope, and extremely compact morphology (effective radius $r_e = 4.0^{+1.4}_{-1.4}$ pc). These properties are consistent with massive star formation in a pristine or near-pristine environment. The finding of such an example at a relatively late time in cosmic history is surprising. However, regardless of cosmic epoch, the identification of a potentially pristine object is a key validation of the Big Bang model.

The doubly lensed system “33.1a/b” was first observed with VLT/MUSE [6]. Residing behind the Abell 2744 galaxy cluster, the source is strongly gravitationally lensed and displays two images to the west of the foreground galaxy cluster. Ly α emission was detected at the position, establishing its redshift as $z = 5.725$. The same field has been repeatedly observed with the JWST since the beginning of its science operation as part of multiple programs [7–10]. An RGB mosaic image using the NIRCcam data is shown in Figure 1, where we highlight the positions of the double system, which we nickname “Abell2744 Metal-poor Object REdshift 6”, or “AMORE6.”

We analyzed public NIRCcam WFSS data from Cycle 3 program “All the Little Things” (GO 3516; PIs: Matthee & Naidu) [11], which targeted the Abell 2744 field using the F356W+GRISM configuration. These observations provide wavelength coverage of 3–4 μm at the position of AMORE6. Spectra at both image positions are obtained from two sets of exposures taken at slightly different position angles (PAs; 56° and 60°). For each source, we extracted spectra separately for the two PAs, and also extracted a combined spectrum at each image position using data from both PAs.

The spectra of the two images (hereafter AMORE6-A and AMORE6-B) are shown in Figure 2. Along the spectral trace at the position of AMORE6-B, we clearly detect an emission line at $\sim 3.271 \mu\text{m}$, matching the expected wavelength of H β based on the Ly α redshift measured by VLT/MUSE. We detect an emission line at the same wavelength in individual spectra at both PAs (Methods, Sec 6). The presence of the emission line at the same wavelength in both spectra firmly attributes the origin to the H β line of AMORE6, not spectral contamination from other nearby sources. Similarly, the H β line is detected in the spectrum of AMORE6-A, the counter image of AMORE6-B. While AMORE6-A is located in a relatively crowded region by two foreground galaxies, the spectra extracted from both PA data sets reveal H β at the expected position as well. Lastly, we combine the 1-dimensional spectra of AMORE6-A and AMORE6-B, correcting each for its respective magnification factor to recover intrinsic flux densities, and stack them using inverse-variance weighting (Figure 2, bottom panel).

Intriguingly, none of the reduced spectra reveal the [O III]-doublet lines (rest-frame $\lambda\lambda 4960, 5008$) at the expected wavelength. The doublet lines are usually very bright ($R3 \equiv [\text{O III}]_{\lambda 5008}/\text{H}\beta \gg 1$) in star-forming galaxies with non-zero metallicity. The absence of [O III] immediately indicates that AMORE6 harbors a very low-metallicity, near pristine, interstellar medium. Using the conservative upper limit derived from

the stack spectrum and strong line calibrations derived from photo-ionization models (see Methods, Section 6), we constrain the oxygen abundance of AMORE6 to $\log(\text{O}/\text{H}) < 6.0$, or $< 0.20\%$ of solar metallicity.

The inferred upper limit to Oxygen abundance is shown in Figure 3 and compared with high-redshift galaxies observed with JWST^[12–17]. Of particular interest is LAP1, a previously reported metal-poor star complex at $z = 6.639$ ^[18]. A recent study^[16] followed up one of the clumps (LAP1-B) with JWST/NIRSpec and detected the [O III]-doublet lines along with other emission lines originated by heavy elements. Compared to LAP1-B, AMORE6 has ~ 0.3 dex lower $\log R3$ and ~ 0.3 dex lower $\log(\text{O}/\text{H})$. For its stellar mass, AMORE6 is placed ~ 1 dex below the mass-metallicity relation derived at the corresponding redshift^[14].

Besides the spectroscopic features revealed above, AMORE6 has several exceptional characteristics, as inferred from the 20-band NIRCам photometry (see Methods). Those are: (i) low stellar mass, (ii) blue UV spectral slope β_{UV} , (iii) high specific star formation rate, (iv) compact morphology, and (v) negative continuum break across the Balmer limit, or “Balmer jump.” AMORE6 is very low-mass ($M_* = 5.6 \times 10^5 M_\odot$), UV faint ($M_{\text{UV}} = -14.5$ ABmag), and blue ($\beta_{\text{UV}} = -2.8$). The derived UV slope of AMORE6 is below the lower limit that can be produced by standard stellar population models ($\beta_{\text{UV}} \sim -2.5$), likely requiring enhanced massive star populations^[19,20]. Using the $\text{H}\beta$ -based star formation rate (SFR), we obtain a high specific star formation rate, $\sim 630 \text{ Gyr}^{-1}$. Such intense star formation activity is consistent with the hypothesis that this galaxy is currently undergoing its first burst of star formation without having been pre-enriched. It is also interesting to note that the inferred stellar mass is compatible to what could be expected in an atomic cooling halo with modest star-formation efficiency. This would be compatible with star formation in a pristine gas cloud. The possible existence of such pristine halos at redshift around 6 (or even lower) was predicted theoretically^[21–24], and this is the best observed candidate so far.

Despite the large magnification, AMORE6 remains compact in the image plane, without showing any obvious extended features or associated clumps. This suggests that AMORE6 is intrinsically very compact, which makes it distinct from previously reported strongly lensed objects at high redshift^[25,26]. Using the F150W image, we estimated an effective radius of $R_e = 4.0^{+1.4}_{-1.4} \text{ pc}$, which is comparable to the characteristic scale of massive star cluster formation^[27,28]. This suggests that AMORE6 resides in extremely dense gas, which is reflected in its exceptionally high stellar mass and SFR surface densities, $\Sigma_* = 5.6 \times 10^4 M_\odot \text{ pc}^{-2}$ and $\Sigma_{\text{SFR}} = 4.0 \times 10^{-2} M_\odot \text{ yr}^{-1} \text{ pc}^{-2}$. Lastly, we note that our spectral energy distribution (SED) model indicates a high contribution by the nebular component over the stellar component, which is expected in a young (a few 10^6 yr), high temperature ($\gtrsim 5 \times 10^4 \text{ K}$) environment^[29,30]. The detection of Balmer jump (Methods) supports the presence of hot ionizing sources^[31], suggesting the dominance of very young stars, formed within the last $\sim 10 \text{ Myr}$. All the observations support the hypothesis that AMORE6 hosts primordial, massive star formation on a very small physical scale, making it the best metal-free galaxy candidate so far.

AMORE6 is observed about one billion years after the Big Bang. Previous studies^[13,14,32–36] have found that galaxies are significantly enriched already at high

redshift, within the first few hundred million years. The finding of a near-pristine object at a relatively late time in cosmic history could be seen as surprising even though it is not entirely unexpected theoretically^[21–24]. Indeed, the existence of objects like AMORE6 is a powerful validation of our galaxy formation and clustering models. We note that near the redshift of AMORE6, there are two overdensities of galaxies along the same sightline, at $z = 5.66$ and $z = 5.78$ ^[37]. As shown in Figure 4, AMORE6 falls in the “empty” space existing between the two *evolved* overdensities, where the aforementioned study found *zero* spectroscopically confirmed galaxies. One possible interpretation is that the gravitational potential towards both overdensities might have kept the space in-between relatively clean of galactic pollution delaying the formation of galaxies therein to this relatively late cosmic time and enabling some objects to remain pristine^[38,39].

The identification of a pristine object represents the confirmation of our models predicting that elements heavier than Helium are made in stars and is a basic validation of the cosmological models for the growth of structure in the Universe. While JWST has shown that many of the details of our models for galaxy formation need to be revised, it has also enabled us to confirm the basic ideas behind those models.

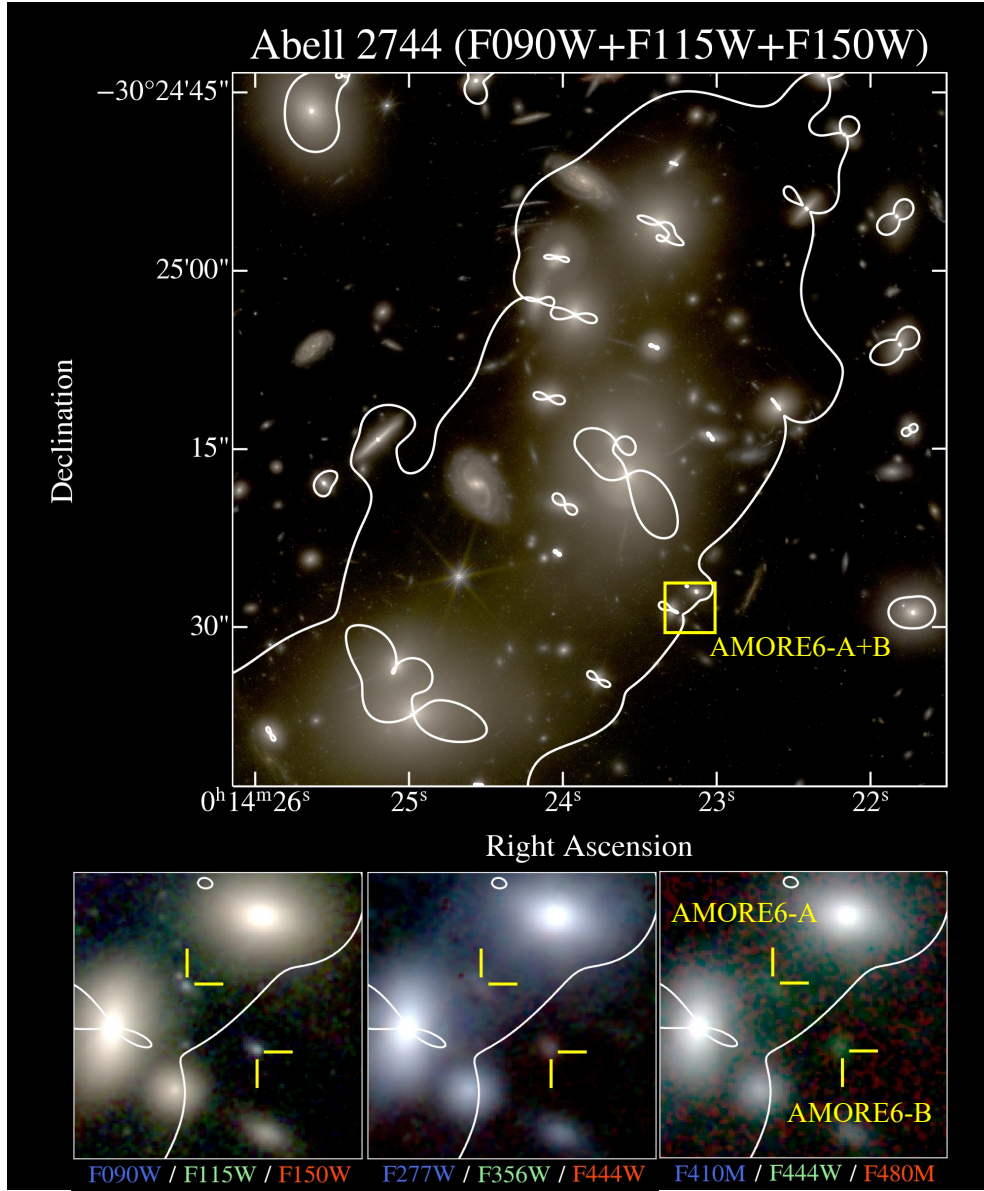


Fig. 1: Mosaic image of the Abell 2744 field. (Top:) The observed position of the AMORE6-A+B system is indicated in the mosaic image (square). The double image system straddles the critical curve predicted from the latest gravitational lens model^[6] (white lines). **(Bottom:)** Zoomed-in cutout images of the AMORE6-A+B system in the size of $4'' \times 4''$, in pseudo RGB colors combined with various NIRCcam filters.

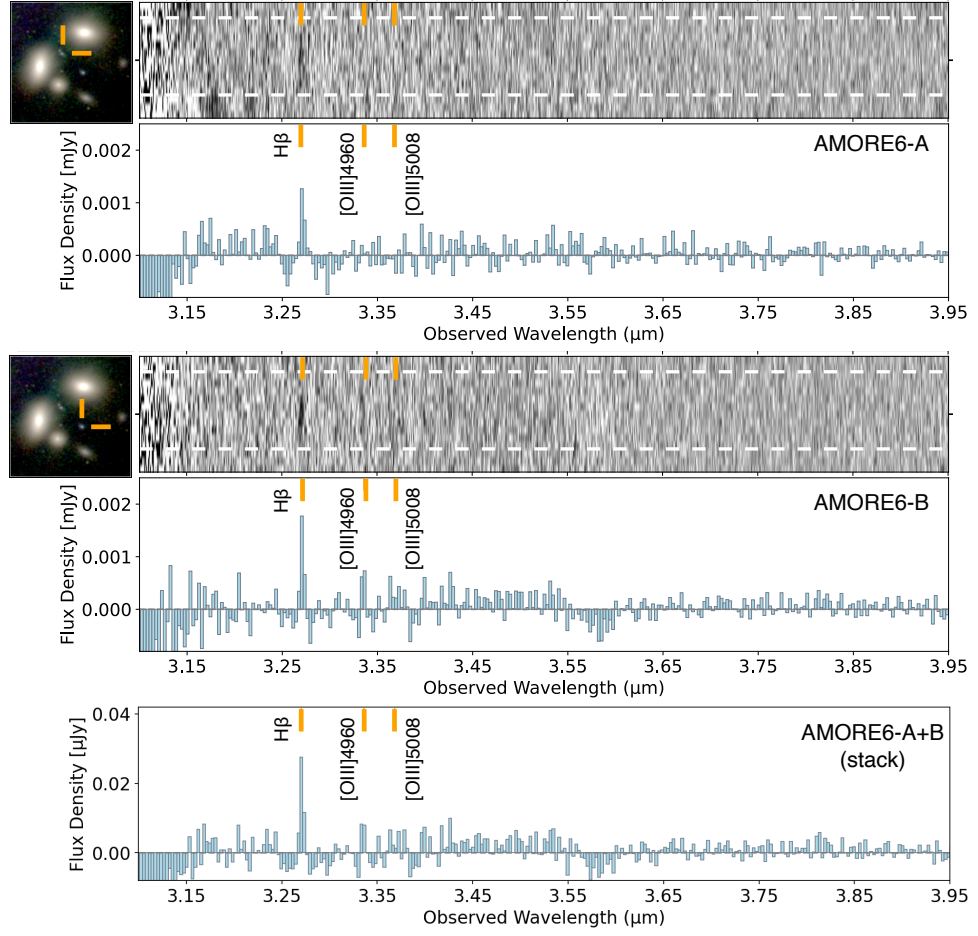


Fig. 2: WFSS spectra of AMORE6. (Top:) Observed WFSS spectrum extracted at the position of AMORE6-A. The top row shows the extracted 2-dimensional spectrum, with contamination being subtracted (see Methods). The bottom row shows the extracted 1-dimensional spectrum, resampled at the spectral bin size of 3 Å. The wavelengths of the $H\beta$ and [O III]-doublet lines are indicated by vertical bars. **(Middle:)** Same as the top panel but for AMORE6-B. **(Bottom:)** 1-dimensional spectrum of the AMORE6-A+B stack spectrum. Each spectrum is normalized by the magnification factor, and thus the final spectrum represents the “unlensed” flux.

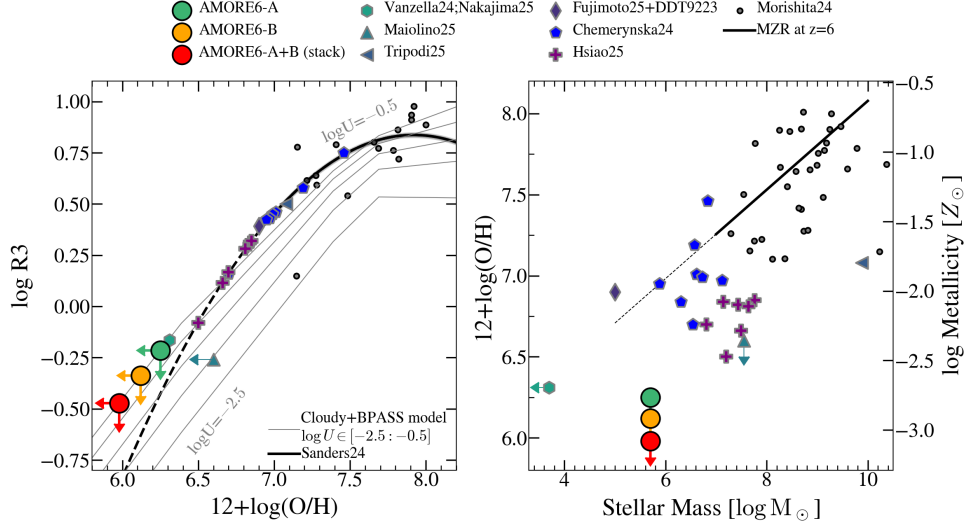


Fig. 3: Oxygen abundance of AMORE6. (Left:) $R3 \equiv [O\text{ III}]_{\lambda 5008}/H\beta$ measurements of AMORE6-A, AMORE6-B, and AMORE6-A+B (stack). Photo-ionization models (gray solid lines in the back ground) are used to infer $\log(O/H)$ as a function of observed $R3$. For comparison, galaxies at $3 < z < 10$ from studies in the literature are shown [14,16,17,40–43], using the reported $R3$ and $\log(O/H)$ measurements (small symbols). (Right:) AMORE6 on the stellar-mass metallicity plane. The same literature galaxies are shown along with the mass-metallicity relation at $z = 6$ [14].

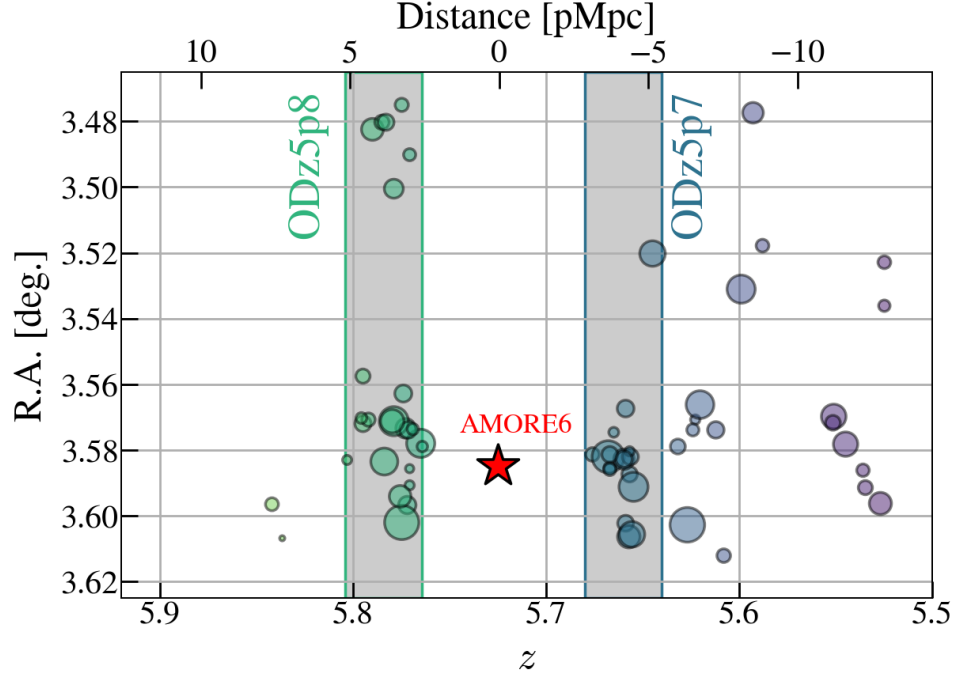


Fig. 4: AMORE6 in the redshift-R.A. space. AMORE6 (red star symbol) is located approximately in the middle of two previously reported galaxy overdensities^[37] at $z = 5.66$ (ODz5p7) and $z = 5.78$ (ODz5p8). The previous study identified no spectroscopic sources in between the two overdensities. The symbol size of galaxies (circles) is scaled by the corresponding stellar mass. Data are adapted from^[37].

Methods

Throughout the manuscript, we adopt a standard Λ CDM cosmology with $\Omega_\Lambda = 0.7$, $\Omega_m = 0.3$, and $H_0 = 70 \text{ km s}^{-1} \text{ Mpc}^{-1}$. All magnitudes are given in the AB magnitude system^[44,45]. The solar metallicity value $12+\log(\text{O}/\text{H}) = 8.69$ ^[46] is adopted throughout this paper.

Imaging Data Reduction

AMORE6 is located behind the galaxy cluster Abell 2744 at $z = 0.308$. This field has been repeatedly observed with JWST since the beginning of its science operation in multiple cycles (see below). We utilize JWST/NIRCam imaging data available in this field from multiple programs: GLASS-JWST (ERS 1324; PI: Treu)^[7], UNCOVER (GO 2561; PI: Labbe)^[47], DD 2756 (PI: Chen)^[48], GO 2883 (PI: Sun), All the Little Things (GO 3516; PIs: Matthee & Naidu)^[11], GO 3538 (PI: Iani), BEACON (GO 3990; PI: Morishita)^[9], and Medium Bands, Mega Science (GO 4111; PI: Suess)^[49].

All NIRCam images of 20 bands are reduced in a consistent way, following^[9]. The JWST pipeline version used for the analysis is ver1.18.0 and the pmap context 1298. We process the images to have the same pixel grid, with the pixel scale of $0.''02$, after registering to the astrometry defined by GAIA DR3. We supplement the data with publicly available deep HST/ACS F435W, F606W, and F814W images^[50].

In summary, we utilize 20 NIRCam and 3 HST bands. The 5σ point source limiting magnitudes: HST-F435W (28.7), F606W (28.1), F814W (27.7), NIRCam-F070W (28.5), F090W (28.9), F115W (28.7), F140M (27.9), F150W (28.8), F162M (27.9), F182M (28.1), F200W (28.9), F210M (28.0), F250M (28.0), F277W (29.1), F300M (28.1), F335M (28.1), F356W (29.1), F360M (28.2), F410M (28.6), F430M (27.7), F444W (28.9), F460M (26.8), F480M (27.2).

Photometry

The reduced images were used for photometry. We identified sources in the rest-frame UV detection image (F150W+F200W stack) using **SExtractor**^[51] and measured flux on each image (matched to the F444W point-spread function, PSF) within a fixed aperture of radius $r = 0.''16$. This study utilizes the F150W+F200W stack image for source detection, as opposed to, e.g., longer wavelength filters often used in the literature. The choice was made because the former offers a $\sim 2\times$ higher spatial resolution, which increases the detection completeness of faint sources in relatively crowded regions, as is the case for AMORE6-B.

AMORE6-A is found in a relatively isolated region, whereas AMORE6-B is observed near two passive, bright, foreground galaxies at $z \sim 0.5$. Besides, we detect a compact object to the North-East of AMORE6-B, which is almost blended in the longer wavelength bands. This compact object shows slightly different colors than AMORE6-B in the RGB images (Figure 1), with photometric redshift $z_{\text{phot}} = 5.5^{+0.3}_{-0.4}$. We did not detect emission lines along its spectral trace (Section 6), while the association of the compact object remains to be confirmed in future observations.

The light profile of AMORE6 is measured in the F115W image, which corresponds to the rest-frame 1700 \AA . We use **galfit** software^[52] and fit the 2-dimensional light

profile in the image plane with a single Sérsic model. AMORE6-B is well characterized with Sérsic index $n = 1$ and a small effective radius $r_e = 34 \text{ mas}$ in the image plane, or $r_e = 2.6^{+0.1}_{-0.1} \text{ pc}$ after correcting for magnification. AMORE6-A, which has a closely located small clump, is also characterized with Sérsic index $n = 1$, but has a slightly larger source-plane radius $r_e = 5.4^{+0.4}_{-0.4} \text{ pc}$ than AMORE6-B's. The source of the discrepancy is unknown but could be due to source confusion at the position of AMORE6-A or differential lens magnification across each image, which may affect the light profile reconstruction in the image plane. Conservatively, we quote the mean size of the two measurements, $r_e = 4.0^{+1.4}_{-1.4} \text{ pc}$, as the characteristic size of AMORE6.

NIRCam WFSS Reduction

We analyzed public NIRCam WFSS data from the Cycle 3 program “All the Little Things” (GO 3516; PIs: Matthee & Naidu)^[11], which provides F356W coverage at the position of AMORE6 over the wavelength range of 3–4 μm . We adopt the median filter technique for continuum subtraction, which has been widely adopted in the literature^[53–55]. This approach models the observed continuum using a moving window (or “kernel”), and subtracts it from the pre-processed 2D spectrum (i.e., flat-fielded and background-subtracted) to effectively isolate the emission line signals.

The spectra were obtained at two slightly different PAs, approximately 56° and 60° . To control the effects of PA dependent spectral overlap from nearby sources (“contamination”), we extracted spectra at the image positions of AMORE6-A and AMORE6-B from each PA individually, as well as from the combined data set including both PAs. This approach allowed us to assess the impact of contamination and to ensure that the detected emission lines are not driven by spurious features present in only one of the orientations. Each PA data set has a total on-source exposure time of 24,738 sec for both positions of AMORE6-A and AMORE6-B.

The reduced spectra of AMORE6 are shown in Figure 2, where we present the combined spectrum of each source. At the position of AMORE6-B, we clearly see the detection of an emission line at $\sim 3.271 \mu\text{m}$, corresponding to $\text{H}\beta$ at $z = 5.725$, consistent with the redshift measured from $\text{Ly}\alpha$ by VLT/MUSE.

In Extended Figures 1 and 2, we also show the individual spectra extracted from each PA. While the spectrum taken at $\text{PA} = 56^\circ$ suffers from significant contamination by a foreground cluster galaxy, the spectrum at $\text{PA} = 60^\circ$ is largely contamination-free (Figure 1). The presence of the emission line at the same wavelength in both spectra firmly attributes the origin to the $\text{H}\beta$ line of AMORE6. In addition, the $\text{H}\beta$ line is detected at the position of AMORE6-A. Although AMORE6-A is located closer to foreground sources and suffers from spectral contamination, $\text{H}\beta$ is detected in all the spectra.

To increase the signal-to-noise ratio (SNR), we combined the 1-dimensional spectra of AMORE6-A and AMORE6-B. Each spectrum was normalized by the magnification factor estimated at the position. The normalized spectra are then stacked by weighting with the inverse variance. The combined spectrum is shown in the bottom panel of Figure 2.

The line profile of each emission line of interest in the extracted 1d spectrum was modeled with a Gaussian function. The amplitude and line width parameters are

included for each line model, in addition to one global redshift parameter. Three lines, $H\beta$, $[O\ III]_{\lambda 4960}$, and $[O\ III]_{\lambda 5008}$, were attempted to fit simultaneously. The fit is iteratively repeated for 5000 times through the Markov chain Monte Carlo method using `emcee` [56]. The integrated flux of each line is estimated by integrating the corresponding Gaussian model, and the flux error is estimated by summing the error weighted by the amplitude of the Gaussian model in quadrature. We detect $H\beta$ in the spectra of AMORE6-A, AMORE6-B, and the AMORE6-A+B stack at SNR of 4.2, 6.2, and 8.3, respectively. Neither one of the $[O\ III]$ lines is detected at $SNR > 3$ in any spectra. The fitting results are shown in Figure 3. The measured line fluxes and flux upper limits are reported in Table 1.

We noticed that the spectrum of AMORE6-B shows 6 consecutive non-zero spectral pixels near the wavelength of $[O\ III]_{\lambda 4960}$ (Figure 2). This corresponds to 2 consecutive spectral pixels in the resampled spectrum (Figure 2). However, the same feature is not consistently seen in the spectrum of AMORE6-A. In addition, the $[O\ III]_{\lambda 4960}$ line is about 3 times fainter than its doublet counterpart, $[O\ III]_{\lambda 5008}$ [57]. The absence of $[O\ III]_{\lambda 5008}$ in all the spectra analyzed here supports the interpretation that the observed positive pixels at the wavelength of $[O\ III]_{\lambda 4960}$ are likely artifacts.

Inference of Oxygen Abundance

Using the measured flux of $H\beta$ and upper limit on $[O\ III]_{\lambda 5008}$, we obtain the oxygen abundance, $12+\log(O/H)$, via strong line calibration methods. The $R3$ calibrator offers a simple conversion between the line ratio $R3 \equiv [O\ III]_{\lambda 5008}/H\beta$ and Oxygen abundance.

Following [16], we ran photo-ionization models using `Cloudy` [58,59] and calculated $R3$ and $\log(O/H)$ in various conditions. We calculate the model for different O/H abundance ratios and ionization parameter ($\log U \in [-2.5 : -0.5]$ in step of 0.5). For hydrogen density, we adopt $n_H = 1000\text{ cm}^{-3}$; however, changing density to 100 cm^{-3} or 10000 cm^{-3} would not significantly affect the final result. For the ionizing source, we use `BPASS` [19,60] binary stellar radiation assuming an instantaneous star formation history with the stellar age of 1 Myr, upper mass cut of $100 M_\odot$, and the Kroupa IMF, of the same metallicity as the gas component. The model grids obtained are comparable to those presented by [16] in the metallicity range of interest.

To determine $\log(O/H)$, we adopted the model of $\log U = -0.5$, the same value as was used for LAP1-B [16]. This ionization parameter was chosen to make a fair comparison with LAP1-B. With this, we obtain $12+\log(O/H) < 6.0$, or $< 0.20\%$ of solar metallicity, for the observed $R3$ measured from the stacked spectrum.

Adopting $\log U = -2.5$ instead, which is the lowest acceptable per observational data in the literature, would increase the oxygen abundance but only by ~ 0.4 dex.

By adopting the strong line calibration published by [33] and extrapolating it down to the $R3$ of AMORE6, we obtained $12+\log(O/H) < 6.2$, or $< 0.32\%$ of solar metallicity. We note that Maiolino et al. [17] adopted the strong line calibration by [61] to obtain their $\log(O/H)$ measurement. This explains their larger measurement than that expected from our approach ($12+\log(O/H) \approx 6.2$) for its relatively low $R3$.

A recent work by [43] selected a candidate Pop-III galaxy using a photometric color-color diagram, followed by a further photometric redshift analysis. The candidate, GLIMPSE-16043, was recently followed up with the JWST/NIRSpec MSA (DDT9223, PI: Fujimoto). We retrieved the reduced G395M/F290LP spectrum from MAST (JWST calibration pipeline ver1.18.0 under the pmap context 1364) and applied our line-fitting analysis. The $H\beta$ and $[O\ III]$ are clearly detected, revealing $\log R3 = 0.39 \pm 0.10$. Using the same Oxygen abundance inference above, we found $12 + \log(O/H) = 6.9$. The object is shown in Figure 3.

Shown in Figure 3 is the mass-metallicity relation, to highlight the location of AMORE6 with respect to galaxies at $3 < z < 10$ [14]. Compared to the mass-metallicity relation at the corresponding redshift [14], AMORE6 falls ~ 1 dex below for its stellar mass.

SED Modeling

We modeled the spectral energy distribution (SED) of AMORE6 using the JWST+HST photometric data. We used the SED fitting code `gsf` ver1.93; [62], which allows flexible determinations of the SED by adopting binned star formation histories (often referred to as “non-parametric”), with the age pixels set to [1, 3, 10, 30, 100, 300, 1000] Myrs. The fitting templates were generated using the BPASS template library of a single initial mass function (“imf135_300”), with the upper cutoff mass of $300 M_\odot$, including binary populations. Given our interest, we only included the templates of the lowest metallicity available ($10^{-5} Z_\odot$). In addition, nebular templates for various ionization parameters ($\log U \in [-3.5 : -0.5]$), distributed by the BPASS team, are included to account for the nebular emission and continuum component. The nebular templates are also set to the same metallicity as for the stellar templates. For dust attenuation, we adopted the SMC dust curve [63]. In summary, our SED modeling has 7 (amplitudes for stellar templates) + 2 (amplitude and ionization parameter for nebular templates) + 1 (dust attenuation) parameters.

The SED fitting was performed on AMORE6-A and AMORE6-B separately. The measurements for AMORE6-A suffer from larger uncertainties, probably due to its location near bright galaxies as well as its smaller magnification factor. The physical quantities of AMORE6 are thus represented by using the measurements of AMORE6-B throughout the manuscript. Physical quantities are reported in Table 2. The star formation rate is calculated using the $H\beta$ flux measured in Section 6 and the following relation [64]:

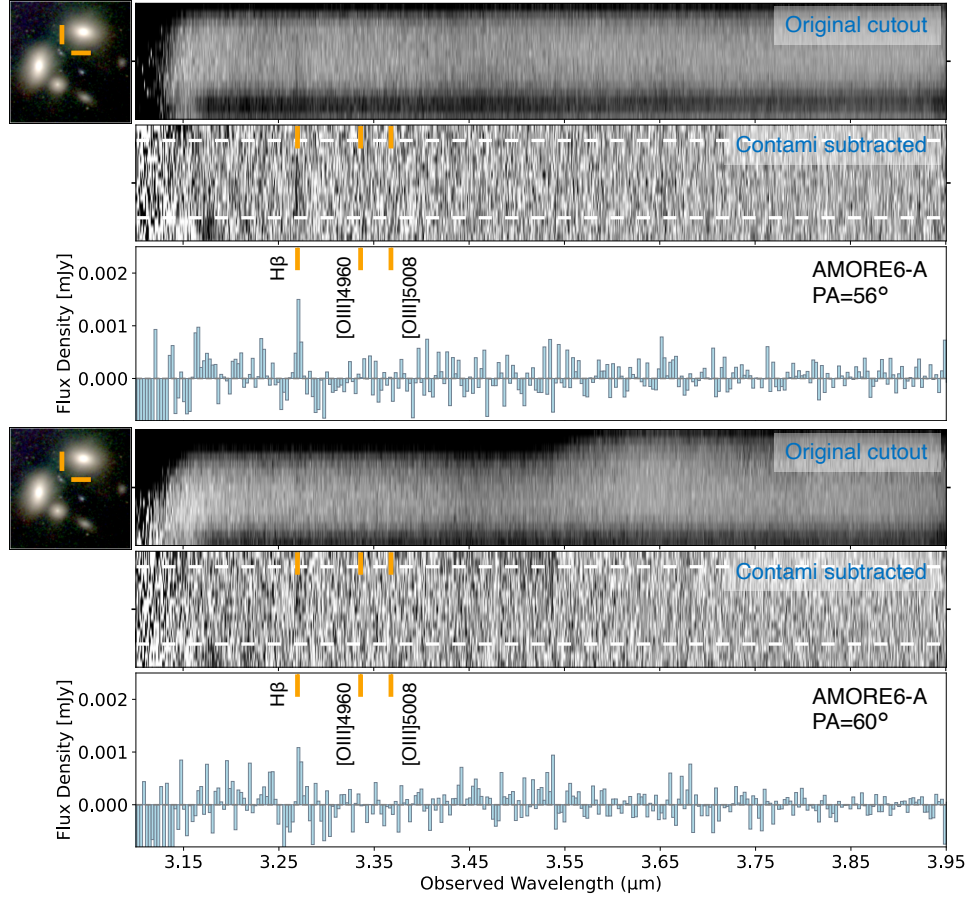
$$\text{SFR} [M_\odot \text{ yr}^{-1}] = 7.9 \times 10^{-42} L_{H\alpha} [\text{erg s}^{-1}], \quad (1)$$

where $L_{H\alpha} = 2.86 \times L_{H\beta}$, assuming Case B recombination with $T_e = 10^4$ K and $n_e = 10^2 \text{ cm}^{-3}$ [58].

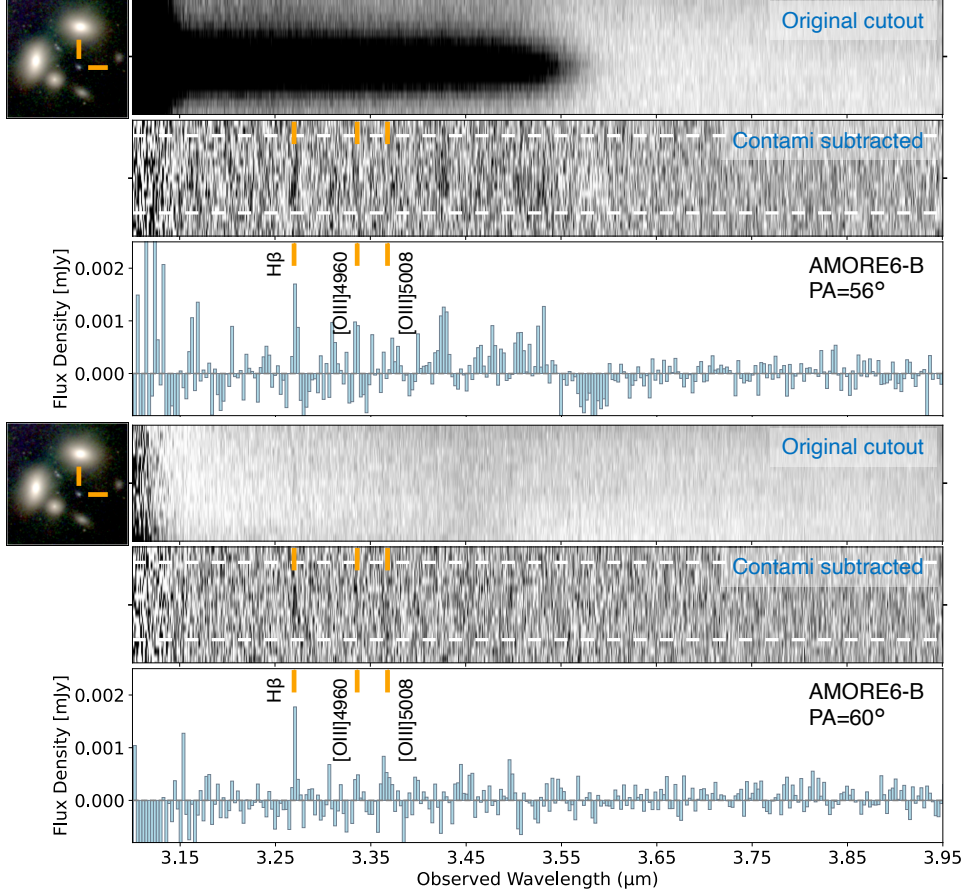
The SED of AMORE6 is characterized by a very young stellar population. Remarkably, the best-fit model shows a large flux contribution from the nebular component, e.g., $\sim 10\%$ at the rest-frame 2000 \AA and $\sim 30\%$ at 3500 \AA . A large nebular contribution is suggestive of young stellar populations in an extremely high-temperature gas, as discussed in the main text [30]. In addition, the observed photometric flux appears to show a discontinuity at the observed wavelengths range $\sim 2 \mu\text{m}$ to $3 \mu\text{m}$, as highlighted in Figure 4. Such a negative continuum break is recognized as the Balmer jump,

observed across the Balmer limit (rest frame 3645 Å), and is another proxy of massive star formation in metal-poor gas clouds^[29,65]. To assess the amplitude of the jump, we measured the mean flux across the Balmer limit using the photometric bands. The blue (measured using the F182M/F200W/F210M bands) and red (F250M/F277W/F300M) fluxes are measured as $0.023 \pm 0.005 \mu\text{Jy}$ and $0.015 \pm 0.005 \mu\text{Jy}$, giving us the flux ratio $f_{\nu,\text{blue}}/f_{\nu,\text{red}} = 1.53 \pm 0.37$. Such a high flux ratio can only be reproduced by a young stellar population ($\lesssim 10$ Myr), according to the calculation using the aforementioned BPASS stellar library or the Pop-III stellar library by^[31].

Extended Data



Extended Data Figure 1: Spectra of AMORE6 from individual roll angles. Same as Figure 2 but for spectra of AMORE6-A from individual roll angle data sets, 56° (top) and 60° (bottom).



Extended Data Figure 2: Spectra of AMORE6 from individual roll angles (continued). Same as Extended Data Figure 1 but for spectra of AMORE6-B.

Acknowledgements

We acknowledge the teams of the JWST observation programs, IDs 1324, 2561, 2756, 2883, 3516, 3538, 3990, and 4111 for their dedicated work in designing and planning these programs and for generously making their data publicly available. Some/all of the data presented in this paper were obtained from the Mikulski Archive for Space Telescopes (MAST) at the Space Telescope Science Institute. TM received support from NASA through the STScI grants HST-GO-17231 and JWST-GO-3990. MS acknowledges support for this work under NASA grant 80NSSC22K1294. ZL is supported by the Japan Society for the Promotion of Science (JSPS) through KAKENHI Grant No. 24KJ0394.

Software: Astropy^[66–68], Cloudy^[58,59], EMCEE^[69], gsf^[62], numpy^[70], JWST pipeline^[71], SExtractor^[51].

Extended Data Table 1: Observed properties of AMORE6-A and AMORE6-B.

Quantity	Unit	AMORE6-A	AMORE6-B	AMORE6-A+B
R.A.	degree	$3.584723e+00$	$3.584413e+00$	–
Decl.	degree	$-3.040316e+01$	$-3.040340e+01$	–
μ		$39.32^{+3.73}_{-3.48}$	$77.69^{+8.37}_{-5.92}$	1^\dagger
R_e	pc	$5.35^{+0.40}_{-0.40}$	$2.56^{+0.12}_{-0.12}$	–
$12 + \log(\text{O}/\text{H})$		< 6.25	< 6.12	< 5.98
R3		< 0.61	< 0.46	< 0.34
$z(\text{H}\beta)$		$5.7253^{+0.0016}_{-0.0008}$	$5.7253^{+0.0005}_{-0.0005}$	$5.7253^{+0.0005}_{-0.0005}$
$f(\text{Hb}_{4862})$	$10^{-19} \text{ erg/s/cm}^2$	21.12 ± 5.06	31.70 ± 5.14	0.50 ± 0.06
$f([\text{OIII}]_{4960})$	$10^{-19} \text{ erg/s/cm}^2$	< 3.23	< 4.21	< 0.06
$f([\text{OIII}]_{5008})$	$10^{-19} \text{ erg/s/cm}^2$	< 3.51	< 5.31	< 0.05

Quoted errors and upper limits are 1σ . \dagger : The stacked spectrum AMORE6-A+B was normalized by the magnification factor before being stacked.

Extended Data Table 2: Physical properties of AMORE6

Property	Unit	Measurement
Stellar mass M_*	$\log M_\odot$	$5.6^{+0.2}_{-0.1}$
Absolute UV magnitude M_{UV}	mag	$-14.52^{+0.07}_{-0.08}$
UV slope β_{UV}		$-2.77^{+0.07}_{-0.09}$
Star formation rate $\text{SFR}_{\text{H}\beta}$	$\log M_\odot \text{yr}^{-1}$	$-0.46^{+0.07}_{-0.08}$

Measurements are corrected for magnification using $\mu = 77.7^{[6]}$.

Author contributions

T.M. led the JWST data reduction and the main analysis and wrote the manuscript. Z.L. led the JWST NIRCам WFSS reduction and the analysis and wrote the manuscript. M.S. contributed to the analysis and to the scientific discussion and wrote the manuscript. T.T contributed to the scientific discussion and wrote the manuscript. P.B. contributed to the lens analysis of the main target and calculated magnification factors at the positions of the two images. Y.Z. contributed to the photoionization models used for the oxygen abundance inference. All authors contributed to the discussion of results and to the final editing of the manuscript.

References

- [1] Curtis-Lake, E. *et al.* Spectroscopic confirmation of four metal-poor galaxies at $z = 10.3\text{--}13.2$. *Nature Astronomy* **7**, 622–632 (2023).
- [2] Bunker, A. J. *et al.* JADES NIRSpec Spectroscopy of GN-z11: Lyman- α emission and possible enhanced nitrogen abundance in a $z = 10.60$ luminous galaxy. *A&A*

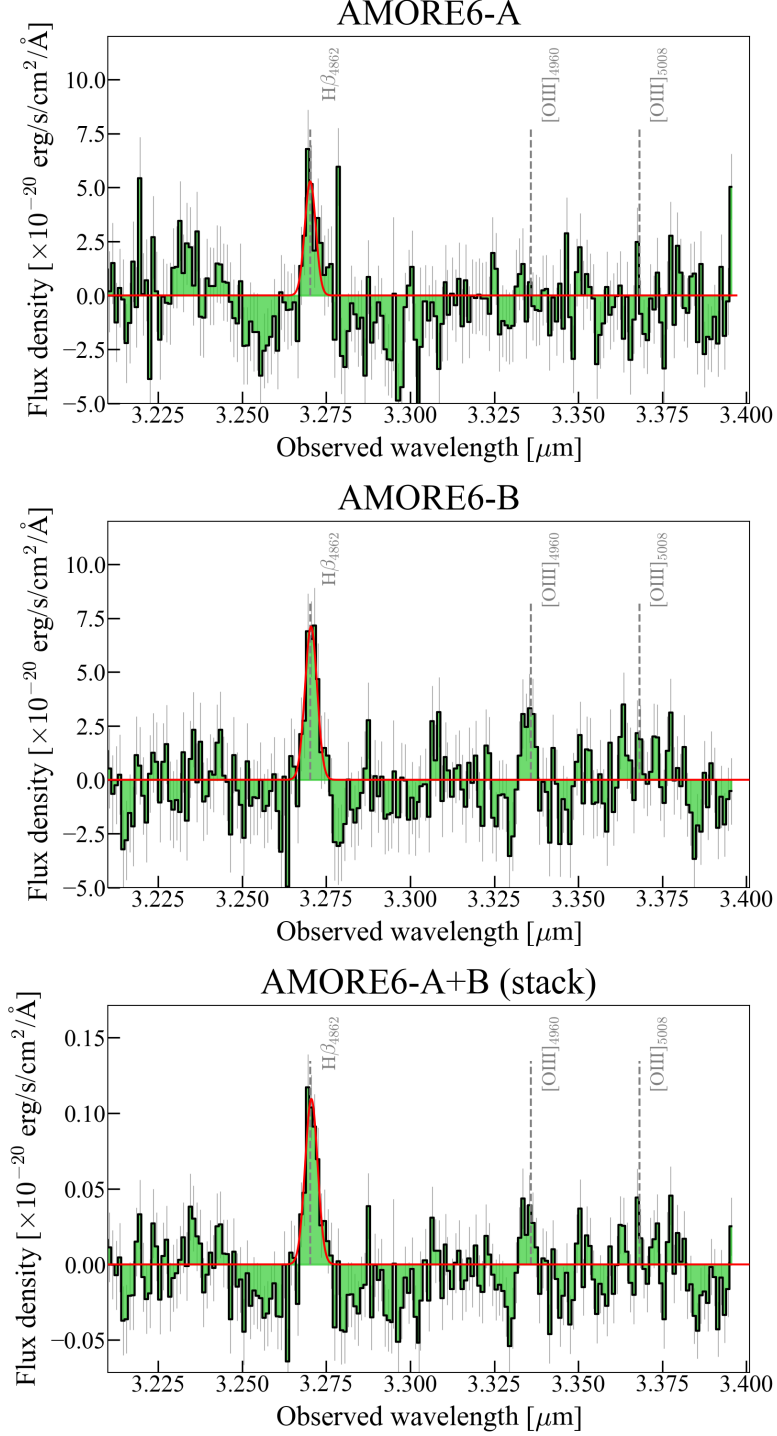
- 677**, A88 (2023).
- [3] Castellano, M. *et al.* JWST NIRSpec Spectroscopy of the Remarkable Bright Galaxy GHZ2/GLASS-z12 at Redshift 12.34. *ApJ* **972**, 143 (2024).
 - [4] Carniani, S. *et al.* Spectroscopic confirmation of two luminous galaxies at a redshift of 14. *Nature* **633**, 318–322 (2024).
 - [5] Naidu, R. P. *et al.* A Cosmic Miracle: A Remarkably Luminous Galaxy at $z_{\text{spec}} = 14.44$ Confirmed with JWST. *arXiv e-prints* arXiv:2505.11263 (2025).
 - [6] Bergamini, P. *et al.* New high-precision strong lensing modeling of Abell 2744. Preparing for JWST observations. *A&A* **670**, A60 (2023).
 - [7] Treu, T. *et al.* The GLASS-JWST Early Release Science Program. I. Survey Design and Release Plans. *ApJ* **935**, 110 (2022).
 - [8] Labbe, I. *et al.* UNCOVER: Candidate Red Active Galactic Nuclei at $3 < z < 7$ with JWST and ALMA. *arXiv e-prints* arXiv:2306.07320 (2023).
 - [9] Morishita, T. *et al.* BEACON: JWST NIRCам Pure-parallel Imaging Survey. I. Survey Design and Initial Results. *ApJ* **983**, 152 (2025).
 - [10] Fu, S. *et al.* Medium-band Astrophysics with the Grism of NIRCам In Frontier fields (MAGNIF): Spectroscopic Census of H α Luminosity Functions and Cosmic Star Formation at $z \sim 4.5$ and 6.3. *arXiv e-prints* arXiv:2503.03829 (2025).
 - [11] Naidu, R. P. *et al.* All the Little Things in Abell 2744: >1000 Gravitationally Lensed Dwarf Galaxies at $z = 0 - 9$ from JWST NIRCам Grism Spectroscopy. *arXiv e-prints* arXiv:2410.01874 (2024).
 - [12] Nakajima, K. & Maiolino, R. Diagnostics for PopIII galaxies and direct collapse black holes in the early universe. *MNRAS* **513**, 5134–5147 (2022).
 - [13] Laseter, I. H. *et al.* JADES: Detecting [OIII] $\lambda 4363$ emitters and testing strong line calibrations in the high- z Universe with ultra-deep JWST/NIRSpec spectroscopy up to $z \sim 9.5$. *A&A* **681**, A70 (2024).
 - [14] Morishita, T. *et al.* Diverse Oxygen Abundance in Early Galaxies Unveiled by Auroral Line Analysis with JWST. *ApJ* **971**, 43 (2024).
 - [15] Chakraborty, P. *et al.* Unveiling the Cosmic Chemistry II: “direct” T_e -based metallicity of galaxies at $3 < z < 10$ with JWST/NIRSpec. *arXiv e-prints* arXiv:2412.15435 (2024).
 - [16] Nakajima, K. *et al.* An Ultra-Faint, Chemically Primitive Galaxy Forming at the Epoch of Reionization. *arXiv e-prints* arXiv:2506.11846 (2025).

- [17] Maiolino, R. *et al.* A black hole in a near-pristine galaxy 700 million years after the Big Bang. *arXiv e-prints* arXiv:2505.22567 (2025).
- [18] Vanzella, E. *et al.* An extremely metal-poor star complex in the reionization era: Approaching Population III stars with JWST. *A&A* **678**, A173 (2023).
- [19] Eldridge, J. J. *et al.* Binary Population and Spectral Synthesis Version 2.1: Construction, Observational Verification, and New Results. *PASA* **34**, e058 (2017).
- [20] Schaerer, D., Marques-Chaves, R., Xiao, M. & Korber, D. Discovery of a new N-emitter in the epoch of reionization. *A&A* **687**, L11 (2024).
- [21] Schneider, R., Salvaterra, R., Ferrara, A. & Ciardi, B. Constraints on the initial mass function of the first stars. *MNRAS* **369**, 825–834 (2006).
- [22] Tornatore, L., Ferrara, A. & Schneider, R. Population III stars: hidden or disappeared? *MNRAS* **382**, 945–950 (2007).
- [23] Trenti, M., Stiavelli, M. & Shull, J. M. Metal-free Gas Supply at the Edge of Reionization: Late-epoch Population III Star Formation. *ApJ* **700**, 1672–1679 (2009).
- [24] Bovill, M. S., Stiavelli, M., Wiggins, A. I., Ricotti, M. & Trenti, M. Kindling the First Stars. I. Dependence of Detectability of the First Stars with JWST on the Population III Stellar Masses. *ApJ* **962**, 49 (2024).
- [25] Welch, B. *et al.* A highly magnified star at redshift 6.2. *Nature* **603**, 815–818 (2022).
- [26] Fujimoto, S. *et al.* Primordial Rotating Disk Composed of ≥ 15 Dense Star-Forming Clumps at Cosmic Dawn. *arXiv e-prints* arXiv:2402.18543 (2024).
- [27] Krumholz, M. R. *et al.* Beuther, H., Klessen, R. S., Dullemond, C. P. & Henning, T. (eds) *Star Cluster Formation and Feedback*. (eds Beuther, H., Klessen, R. S., Dullemond, C. P. & Henning, T.) *Protostars and Planets VI*, 243–266 (2014). [1401.2473](#).
- [28] Polak, B. *et al.* Massive star cluster formation: I. High star formation efficiency while resolving feedback of individual stars. *A&A* **690**, A94 (2024).
- [29] Panagia, N., Stiavelli, M., Ferguson, H. & Stockman, H. S. Avila-Reese, V., Firmani, C., Frenk, C. S. & Allen, C. (eds) *Observational Properties of Primordial Stellar Populations*. (eds Avila-Reese, V., Firmani, C., Frenk, C. S. & Allen, C.) *Revista Mexicana de Astronomia y Astrofisica Conference Series*, Vol. 17 of *Revista Mexicana de Astronomia y Astrofisica Conference Series*, 230–234 (2003). [astro-ph/0209278](#).

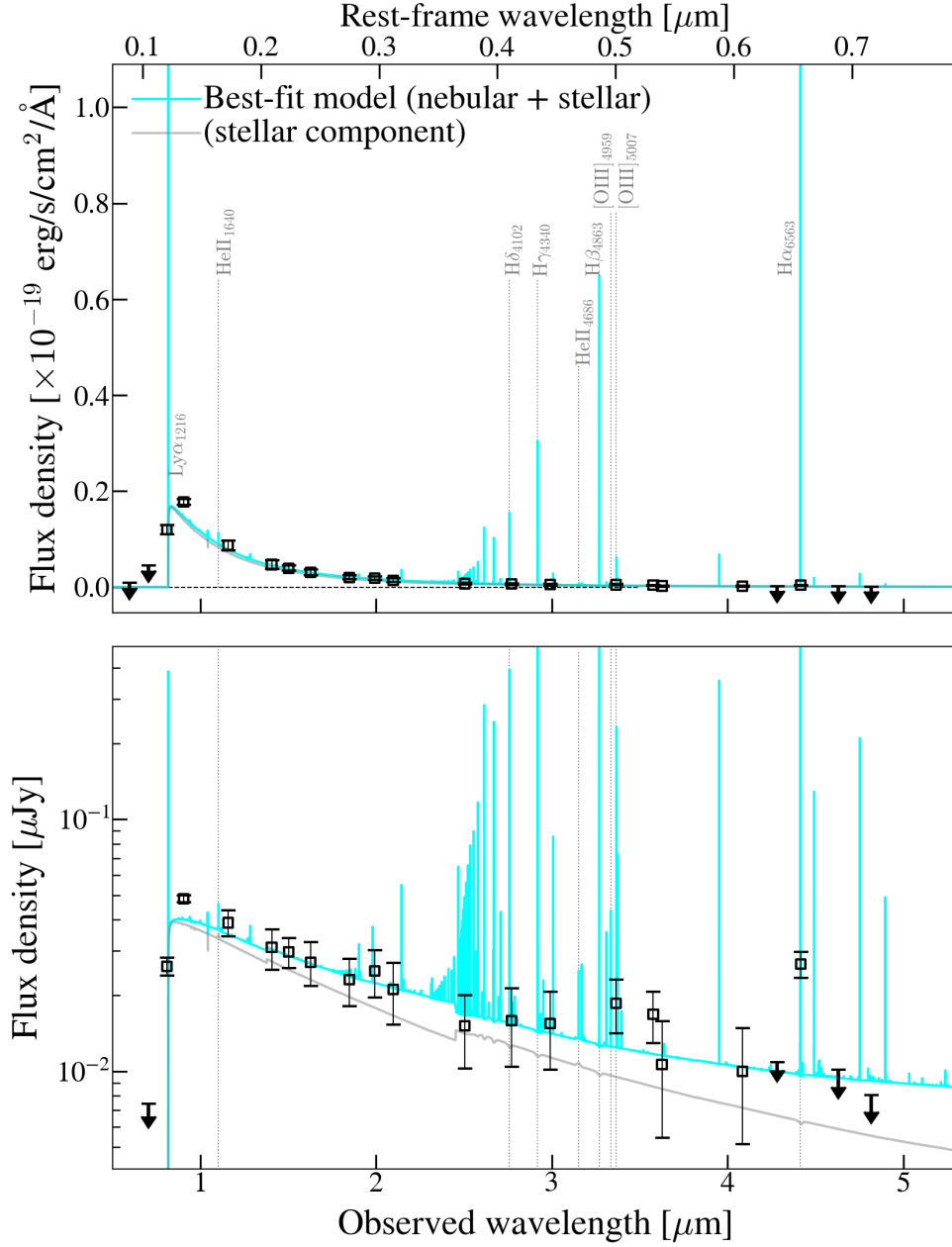
- [30] Katz, H. *et al.* 21 Balmer Jump Street: The Nebular Continuum at High Redshift and Implications for the Bright Galaxy Problem, UV Continuum Slopes, and Early Stellar Populations. *arXiv e-prints* arXiv:2408.03189 (2024).
- [31] Zackrisson, E., Rydberg, C.-E., Schaerer, D., Östlin, G. & Tuli, M. The Spectral Evolution of the First Galaxies. I. James Webb Space Telescope Detection Limits and Color Criteria for Population III Galaxies. *ApJ* **740**, 13 (2011).
- [32] Nakajima, K. *et al.* JWST Census for the Mass-Metallicity Star-Formation Relations at $z=4-10$ with the Self-Consistent Flux Calibration and the Proper Metallicity Calibrators. *arXiv e-prints* arXiv:2301.12825 (2023).
- [33] Sanders, R. L., Shapley, A. E., Topping, M. W., Reddy, N. A. & Brammer, G. B. Direct T_e -based Metallicities of $z = 2-9$ Galaxies with JWST/NIRSpec: Empirical Metallicity Calibrations Applicable from Reionization to Cosmic Noon. *ApJ* **962**, 24 (2024).
- [34] Stiavelli, M. *et al.* The Puzzling Properties of the MACS1149-JD1 Galaxy at $z = 9.11$. *ApJ* **957**, L18 (2023).
- [35] Heintz, K. E. *et al.* The Gas and Stellar Content of a Metal-poor Galaxy at $z = 8.496$ as Revealed by JWST and ALMA. *ApJ* **944**, L30 (2023).
- [36] Curti, M. *et al.* JADES: Insights on the low-mass end of the mass-metallicity-star-formation rate relation at $3 < z < 10$ from deep JWST/NIRSpec spectroscopy. *arXiv e-prints* arXiv:2304.08516 (2023).
- [37] Morishita, T. *et al.* Accelerated Emergence of Evolved Galaxies in Early Overdensities at $z \sim 5.7$. *ApJ* **982**, 153 (2025).
- [38] Stiavelli, M. & Trenti, M. The Clustering Properties of the First Galaxies. *ApJ* **716**, L190–L194 (2010).
- [39] Xu, H., Wise, J. H. & Norman, M. L. Population III Stars and Remnants in High-redshift Galaxies. *ApJ* **773**, 83 (2013).
- [40] Chemerynska, I. *et al.* The Extreme Low-mass End of the Mass-Metallicity Relation at $z \sim 7$. *ApJ* **976**, L15 (2024).
- [41] Tripodi, R. *et al.* Red, hot, and very metal poor: extreme properties of a massive accreting black hole in the first 500 Myr. *arXiv e-prints* arXiv:2412.04983 (2024).
- [42] Hsiao, T. Y.-Y. *et al.* SAPPHIRES: Extremely Metal-Poor Galaxy Candidates with $12 + \log(\text{O}/\text{H}) < 7.0$ at $z \sim 5 - 7$ from Deep JWST/NIRCam Grism Observations. *arXiv e-prints* arXiv:2505.03873 (2025).
- [43] Fujimoto, S. *et al.* GLIMPSE: An ultra-faint $\simeq 10^5 M_\odot$ Pop III Galaxy Candidate and First Constraints on the Pop III UV Luminosity Function at $z \simeq 6 - 7$. *arXiv*

- e-prints* arXiv:2501.11678 (2025).
- [44] Oke, J. B. & Gunn, J. E. Secondary standard stars for absolute spectrophotometry. *ApJ* **266**, 713–717 (1983).
 - [45] Fukugita, M. *et al.* The Sloan Digital Sky Survey Photometric System. *AJ* **111**, 1748 (1996).
 - [46] Asplund, M., Grevesse, N., Sauval, A. J. & Scott, P. The Chemical Composition of the Sun. *ARA&A* **47**, 481–522 (2009).
 - [47] Bezanson, R. *et al.* The JWST UNCOVER Treasury Survey: Ultradeep NIRSpec and NIRCам Observations before the Epoch of Reionization. *ApJ* **974**, 92 (2024).
 - [48] Chen, W. *et al.* Discovery of Candidate Supernova Adjacent to a Galaxy at Redshift $z = 3.47$ in JWST GLASS NIRISS pre-imaging. *Transient Name Server AstroNote* **166**, 1 (2022).
 - [49] Suess, K. A. *et al.* Medium Bands, Mega Science: a JWST/NIRCам Medium-Band Imaging Survey of Abell 2744. *arXiv e-prints* arXiv:2404.13132 (2024).
 - [50] Shipley, H. V. *et al.* HFF-DeepSpace Photometric Catalogs of the 12 Hubble Frontier Fields, Clusters, and Parallels: Photometry, Photometric Redshifts, and Stellar Masses. *ApJS* **235**, 14 (2018).
 - [51] Bertin, E. & Arnouts, S. SExtractor: Software for source extraction. *A&AS* **117**, 393–404 (1996).
 - [52] Peng, C. Y., Ho, L. C., Impey, C. D. & Rix, H.-W. Detailed Structural Decomposition of Galaxy Images. *AJ* **124**, 266–293 (2002).
 - [53] Kashino, D. *et al.* EIGER. I. A Large Sample of [O III]-emitting Galaxies at $5.3 < z < 6.9$ and Direct Evidence for Local Reionization by Galaxies. *ApJ* **950**, 66 (2023).
 - [54] Sun, F. *et al.* First Sample of $H\alpha + [O III]\lambda 5007$ Line Emitters at $z < 6$ Through JWST/NIRCам Slitless Spectroscopy: Physical Properties and Line-luminosity Functions. *ApJ* **953**, 53 (2023).
 - [55] Liu, Z., Morishita, T. & Kodama, T. Characterizing Dust Extinction and Spatially Resolved Paschen- α Emission within 97 Galaxies at $1 < z < 1.6$ with JWST NIRCам Slitless Spectroscopy. *arXiv e-prints* arXiv:2406.11188 (2024).
 - [56] Foreman-Mackey, D., Sick, J. & Johnson, B. python-fsps: Python bindings to fsps (v0.1.1) (2014).
 - [57] Storey, P. J. & Zeippen, C. J. Theoretical values for the [OIII] 5007/4959 line-intensity ratio and homologous cases. *MNRAS* **312**, 813–816 (2000).

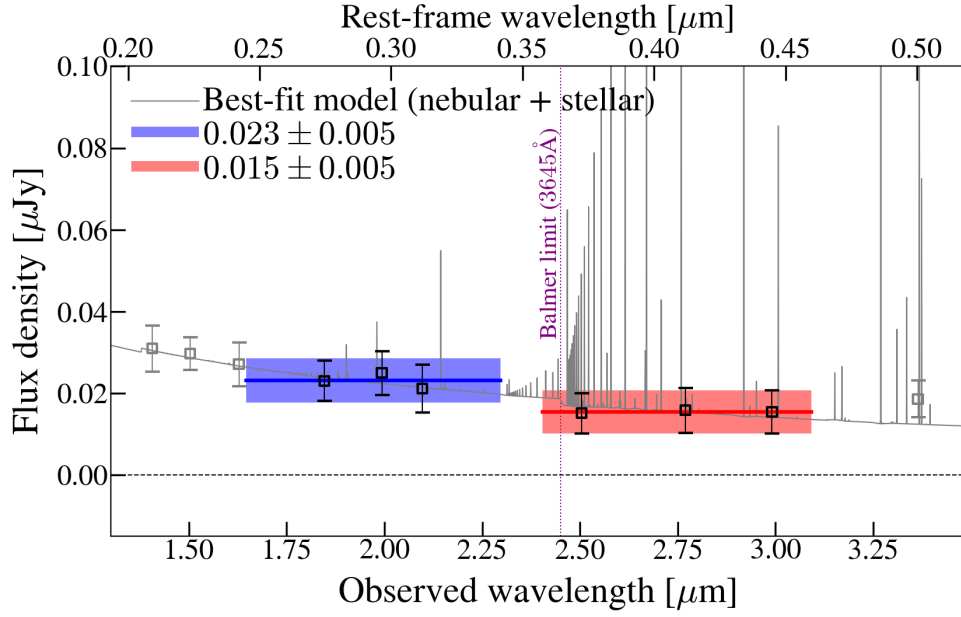
- [58] Osterbrock, D. E. *Astrophysics of gaseous nebulae and active galactic nuclei* (1989).
- [59] Chatzikos, M. *et al.* The 2023 Release of Cloudy. *Rev. Mexicana Astron. Astrofis.* **59**, 327–343 (2023).
- [60] Stanway, E. R. & Eldridge, J. J. Re-evaluating old stellar populations. *MNRAS* **479**, 75–93 (2018).
- [61] Cataldi, E. *et al.* MARTA: Temperature-temperature relationships and strong-line metallicity calibrations from multiple auroral lines detections at cosmic noon. *arXiv e-prints* arXiv:2504.03839 (2025).
- [62] Morishita, T. *et al.* Massive Dead Galaxies at $z=2$ with HST Grism Spectroscopy. I. Star Formation Histories and Metallicity Enrichment. *ApJ* **877**, 141 (2019).
- [63] Gordon, K. D., Clayton, G. C., Misselt, K. A., Landolt, A. U. & Wolff, M. J. A Quantitative Comparison of the Small Magellanic Cloud, Large Magellanic Cloud, and Milky Way Ultraviolet to Near-Infrared Extinction Curves. *ApJ* **594**, 279–293 (2003).
- [64] Kennicutt, J., Robert C. Star Formation in Galaxies Along the Hubble Sequence. *ARA&A* **36**, 189–232 (1998).
- [65] Schaerer, D. On the properties of massive Population III stars and metal-free stellar populations. *A&A* **382**, 28–42 (2002).
- [66] Astropy Collaboration *et al.* Astropy: A community Python package for astronomy. *A&A* **558**, A33 (2013).
- [67] Astropy Collaboration *et al.* The Astropy Project: Building an Open-science Project and Status of the v2.0 Core Package. *AJ* **156**, 123 (2018).
- [68] Astropy Collaboration *et al.* The Astropy Project: Sustaining and Growing a Community-oriented Open-source Project and the Latest Major Release (v5.0) of the Core Package. *ApJ* **935**, 167 (2022).
- [69] Foreman-Mackey, D., Hogg, D. W., Lang, D. & Goodman, J. emcee: The MCMC Hammer. *PASP* **125**, 306–312 (2013).
- [70] Harris, C. R. *et al.* Array programming with NumPy. *Nature* **585**, 357–362 (2020). URL <https://doi.org/10.1038/s41586-020-2649-2>.
- [71] Bushouse, H. *et al.* Jwst calibration pipeline (2023). URL <https://doi.org/10.5281/zenodo.7795697>.



Extended Data Figure 3: Zoomed WFSS spectra of AMORE6. (Top): NIR-Cam WFSS spectrum of AMORE6-A in the original spectral resolution (filled regions with error bars). The best-fit gaussian model is shown (red solid line). The wavelengths of the [O III]-doublet lines are indicated (vertical dashed lines). (Middle): Same as the top panel, but for AMORE6-B. The potential origin of positive pixels near the wavelengths of [O III] $_{\lambda 4960}$ is discussed in the main text (Sec. 6). (Bottom): Same as the top panel, but for the AMORE6-A+B stack spectrum. Each spectrum was normalized by magnification before being stacked.



Extended Data Figure 4: Spectral energy distribution of AMORE6. The spectral energy distribution is modeled using the photometry of AMORE6-B. Observed photometric fluxes are shown with 1- σ errors (squares and arrows). The best-fit full spectrum model (nebular+stellar; cyan line) and stellar component model (gray line) are shown, to highlight the large dominance of the nebular component.



Extended Data Figure 5: Balmer continuum jump in the spectral energy distribution of AMORE6. Same as Extended Data Figure 4 but a zoom-in version to illustrate the wavelength near the Balmer limit, rest-frame 3645 Å (vertical dotted line). The blue and red fluxes across the Balmer limit are measured using the photometric bands (F182M, F200W, F210M and F250M, F277W, F300M, respectively; highlighted with black squares).